SUPPORTING INFORMATION

Bottom-up Preparation of Hierarchically Porous MOF-modified Carbon Spheres Derivatives for Efficient Oxygen Reduction

Lulu Chai[a,b,†], Qi Huang[a,†], Cheng Han[a], Xian Wang[a], Linjie Zhang[b,e], Ting-Ting Li[c], Yue Hu[a,*], Jinjie Qian[a,b,*], and Shaoming Huang[a,d,*]

Dedicated to the 60 years of the Fujian Institute of Research on the Structure of Matter.

[a] *Key Laboratory of Carbon Materials of Zhejiang Province, College of Chemistry and Materials Engineering, Wenzhou University, Wenzhou, 325000, China*

[b] *State Key Laboratory of Structural Chemistry, Fujian Institute of Research on the Structure of Matter, Chinese Academy of Sciences, Fuzhou, 350002, China*

[c] *School of Materials Science and Chemical Engineering, Ningbo University, Ningbo, 315211, China*

[d] *School of Materials and Energy, Guangdong University of Technology, Guangzhou, 510006, China*

[e] *Chimie du solide et de l'énergie-Collège de France 11 Place Marcelin Berthelot, Paris, 75005, France*

[†] *These authors contributed equally to this work.*

**To whom correspondence should be addressed: E-mail: jinjieqian@wzu.edu.cn, smhuang@gdut.edu.cn; Tel: +86-577-88373064.*

Table of Content

Experimental Details

Materials Characterization

The microscopic and nanostructured morphologies of all samples are characterized by scanning electron microscopy (SEM, JEOL JSM-6700F), transmission electron microscopy (TEM, FEI Tecnai F20, 200 kV), high-resolution transmission electron microscope and energy dispersive X-ray spectroscopy analyses (HR-TEM and EDS, JEOL JEM-2100F, 200 kV). The phase of samples are studied by powder X-ray diffraction (PXRD, Bruker D8-Advanced with Cu Kα radiation) at 40 kV, 40 mA (λ = 1.5406 Å), Raman microscope (LabRAM HR Evolution, Thermo-Fisher Scientific, Excitation at 532 nm from an argon ion laser) and X-ray photoelectron spectroscopy (XPS, Thermo Scientific ESCALAB 250). N_2 adsorption/desorption isotherms were used to characterize the determine specific surface areas and pore distribution of samples based on the Brunauer-Emmett-Teller method (BET, Micrometrics ASAP 2020 system).

Electrochemical Measurements.

The electrochemical performance of the samples was conducted in a three-electrode system using the Autolab workstation (Metrohm, Swiss) and/or CHI760E electrochemical workstation (CH Instruments, Shanghai) for ORR, which comprise a counter electrode (graphite rod), a reference electrode (Ag/AgCl (3M KCl)) and a working electrode (rotating ring-disk glass-carbon with catalyst, disk diameter is 5.6 mm). The working electrode is prepared by depositing the ink of catalysts. In a typical process to make up the electrode ink, 5 mg CoZn-ZIF/CS-1000 is dissolved in a mixed solvent containing 450 μL EtOH, 50 μL deionized water, and 20 μL Nafion (5%) to form a homogeneous catalyst ink by ultrasonicating for 3 h. Then 20 μL of the as-prepared droplet is deposited onto the surface of GCE electrode and dried at room temperature condition (a mass loading of ~ 0.35 mg cm^{-2}). Before every test, the electrolyte (0.1 M KOH) is pre-purged with pure O_2 for 30 min to make sure it is O_2-saturated. Firstly, scanning 40 cycles of cyclic voltammetry (CV) curves until the signals is stabilized. The linear sweep voltammetry (LSV) is scanning at a potential scan rate of 5 mV s^{-1} at different rotational speeds from 100 to 2500 rpm for ORR. For data analyzing, all the potential are transferred with reference to standard reversible hydrogen electrode (RHE) according to following equation: $E_{RHE} = E_{Ag/AgCl} + 0.964$ V in 0.1 M KOH. To evaluate the active surface area of catalysts, the double-layer capacitance (C_{dl}) is determined by measuring the CV plots in the region

from 1.00 to 1.10 V *vs*. RHE at various scan rate from 5 to 200 mV s^{-1} in N_2-saturated 0.1 M KOH in non-Faradaic potential region. By fitting the current density at 1.15 V *vs*. RHE at various scan rates, the linear trend is observed and equal to the slope of the linear C_{dl}. All electrochemical impedance spectroscopy (EIS) measurement wasrecorded at the same overpotential of 0.6 V *vs*. RHE in the frequency range of 10^{-2}-10^{6} Hz with an amplitude of 5 mV. Electrocatalytic stability is made by using current-time (i-t) chronoamperometric at 0.6 V in O_2-saturated 0.1 M KOH for 10 h.

The electron transfer number (n) and yield of the H_2O_2 intermediate were calculated according to the Koutecky-Levich (K-L) equations (1-2) and RRDE technologies (3-4), as shown in the following equations:

$$1/\mathbf{j} = 1/\mathbf{j_L} + 1/\mathbf{j_K} \tag{1}$$

$$\mathbf{j_L} = \frac{0.2\mathbf{nFC_0D_0}}{\upsilon^{1/6}} \bullet \frac{1}{\omega^{1/2}} = \mathbf{B} \bullet \frac{1}{\omega^{1/2}} \tag{2}$$

$$\mathbf{n} = \frac{4\mathbf{I_d}}{\mathbf{I_d} + \mathbf{I_r}/\mathbf{N}} \tag{3}$$

$$\mathbf{H_2O_2(\%)} = \frac{2\mathbf{I_r}/\mathbf{N}}{|\mathbf{I_d}| + \mathbf{I_r}/\mathbf{N}} \times 100\% \tag{4}$$

In these formulas, J is the experimental current density, J_L is the diffusion-limited current density, and J_K is the kinetic current density, respectively; ω is the rotation speed in rpm (round per minute), F is the Faraday constant (96,485 C mol^{-1}), C_0 is the bulk concentration of oxygen (1.2×10^{-6} mol cm^{-3}), D_0 is the diffusion coefficient of oxygen in 0.1 M KOH (1.9×10^{-5} cm^2 s^{-1}), and υ is the kinetic viscosity (0.01 cm^2 s^{-1}). When the speed of rotation is also represent as rpm, 0.2 is a constant. The n can be extracted from the slope of the K-L plot. Ir is the ring current, I_d is the disk current and N expresses to the collection efficiencyof the ring electrode (0.37).

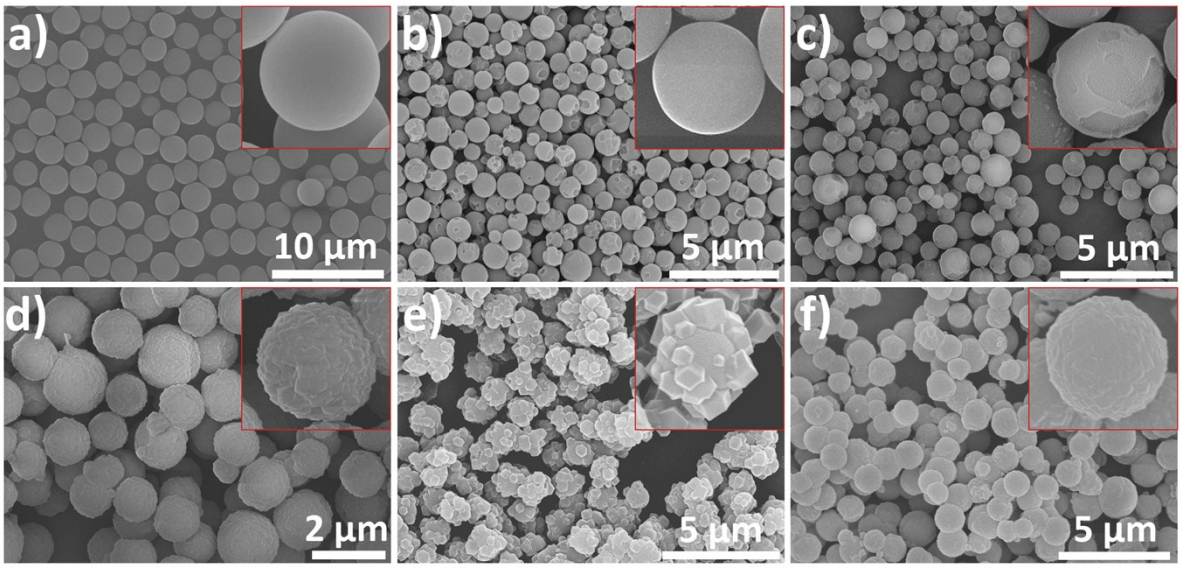

Figure S1. SEM images of (a) poly-disperse **Zn-BTC** spheres; (b) functionalized **CS**; (c) **PDA/CS**; (d) **CoZn-ZIF/CS**; (e) **Co-ZIF/CS**; (f) **Zn-ZIF/CS**;

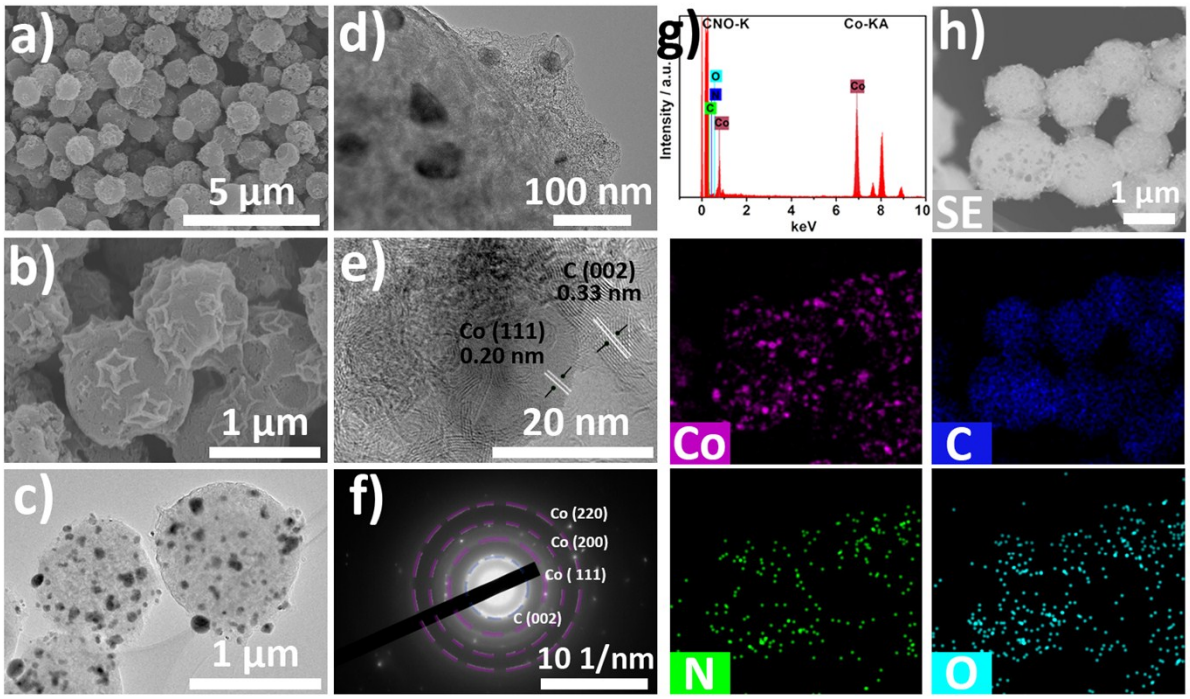

Figure S2. (a, b) SEM, (c) TEM; (d, e) HR-TEM images at different magnification of the **Co-ZIF/CS-1000** spheres, respectively; (f) the corresponding SAED pattern; (g) EDX spectrum; (h) HAADF-STEM image and the corresponding C, N, O, and Co mappings of the **Co-ZIF/CS-1000** spheres.

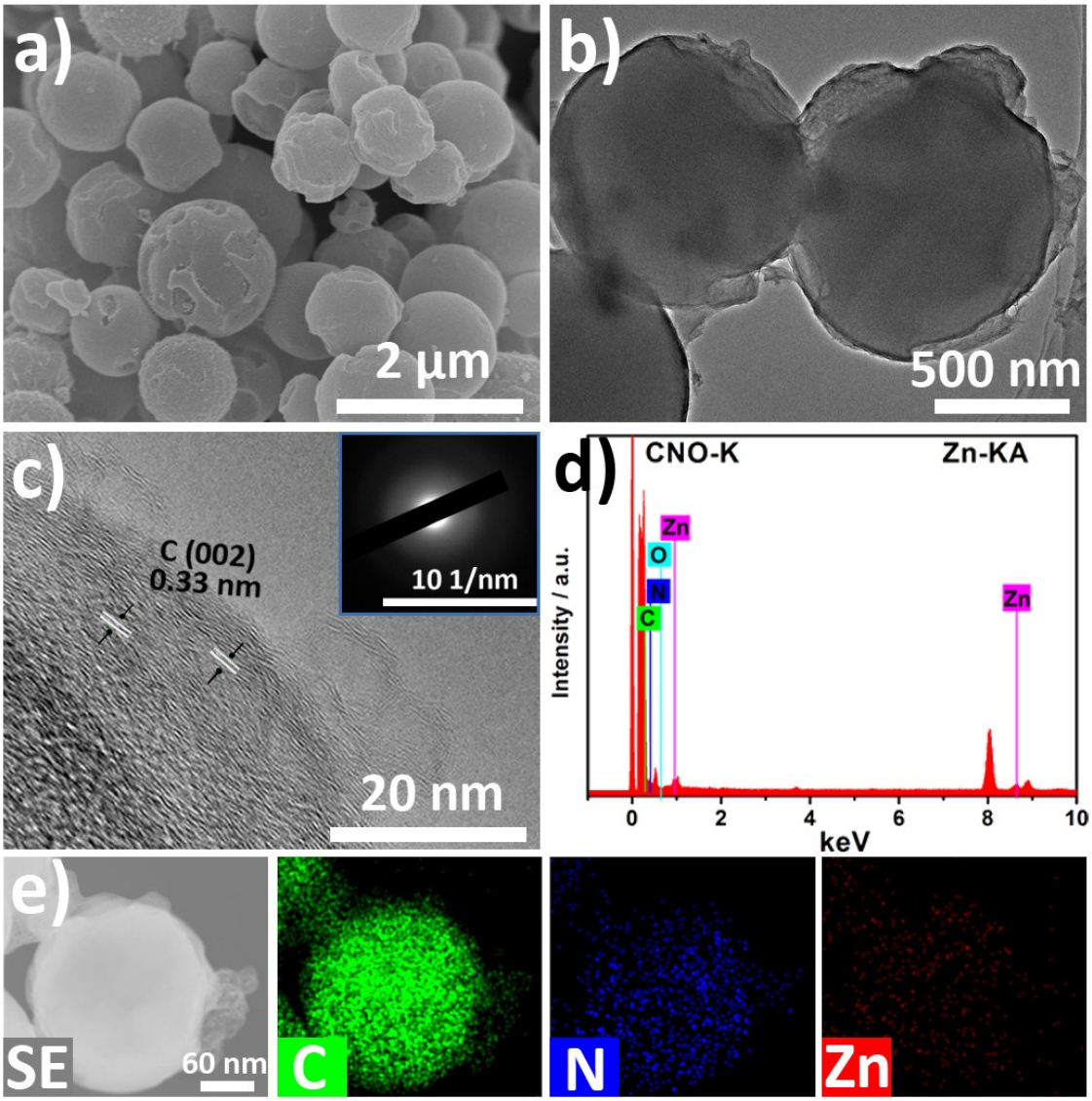

Figure S3. (a) SEM, (b) TEM; (c) HR-TEM images of the **Zn-ZIF/CS-1000** spheres, inset in (c) shows the corresponding SAED pattern; (d) EDX spectrum; (e) HAADF-STEM image and the corresponding C, N, and Zn mappings of the **Zn-ZIF/CS-1000** spheres.

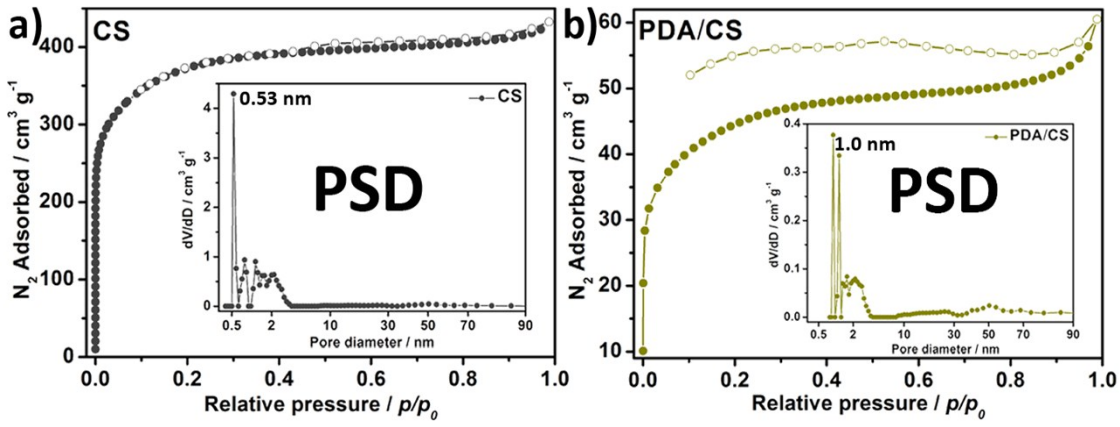

Figure S4. Nitrogen sorption isotherms at 77 K (closed, adsorption; open, desorption) and the corresponding pore size distribution curves of (a) **CS**, (b) **PDA/CS**.

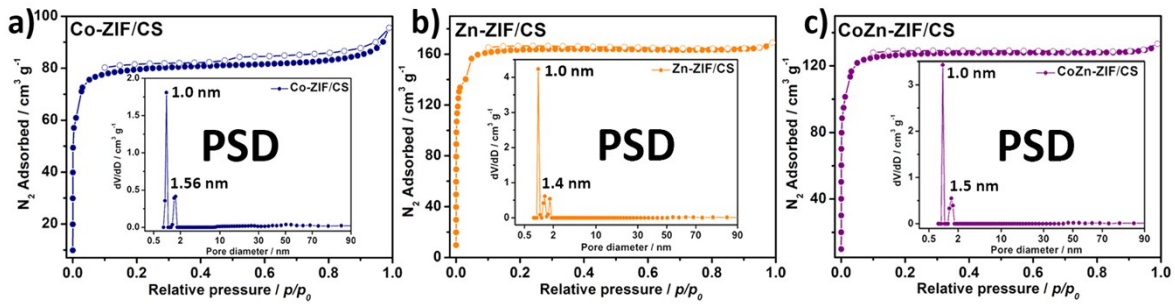

Figure S5. Nitrogen sorption isotherms at 77 K (closed, adsorption; open, desorption) and the corresponding pore size distribution curves of (a) **Co-ZIF/CS**; (b) **Zn-ZIF/CS**; and (c) **CoZn-ZIF/CS**.

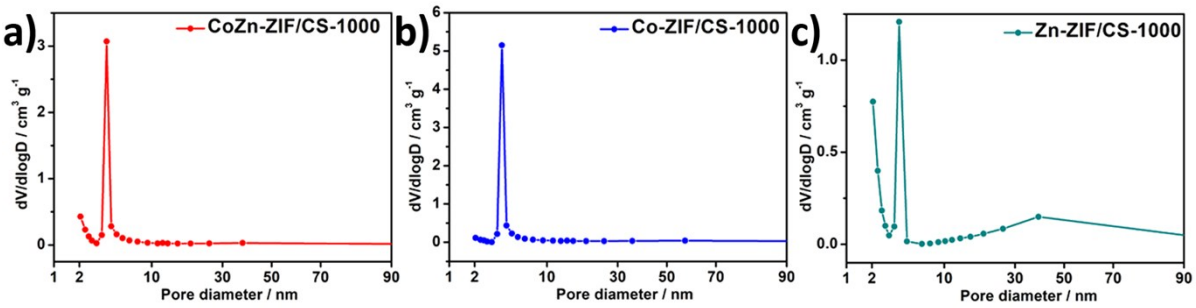

Figure S6. The dV/dlogD curves of CoZn-ZIF/CS-1000, Co-ZIF/CS-1000, and Zn-ZIF/CS-1000.

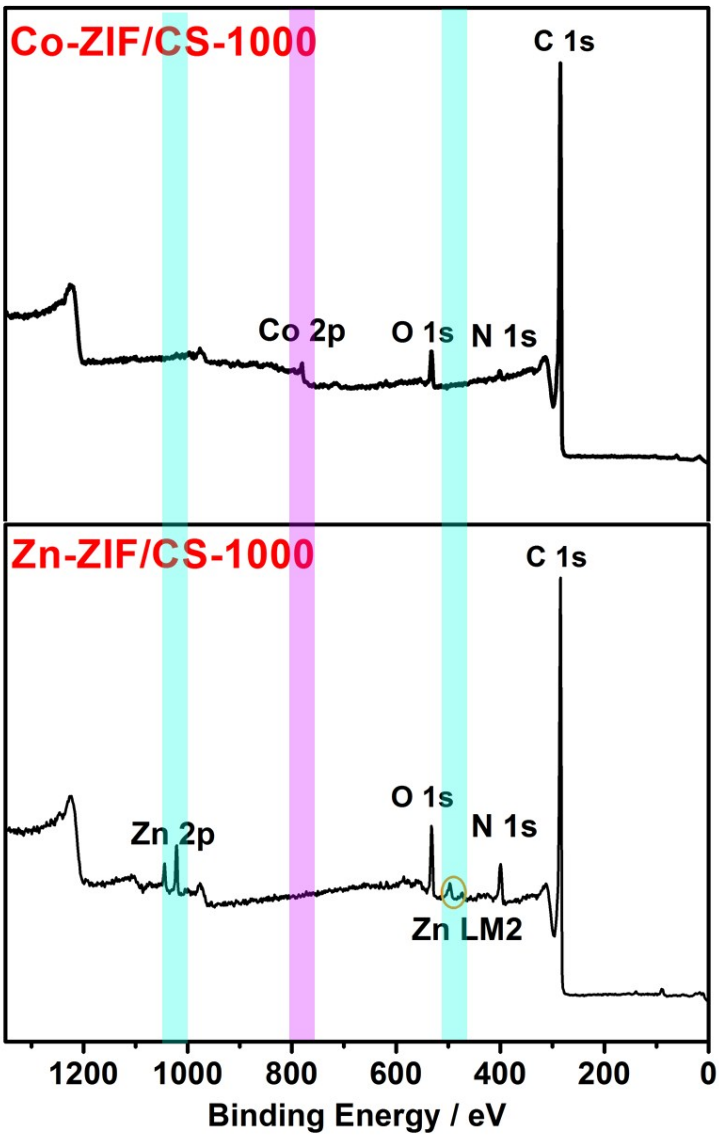

Figure S7. Full survey XPS spectra of **Co-ZIF/CS-1000** and **Zn-ZIF/CS-1000**.

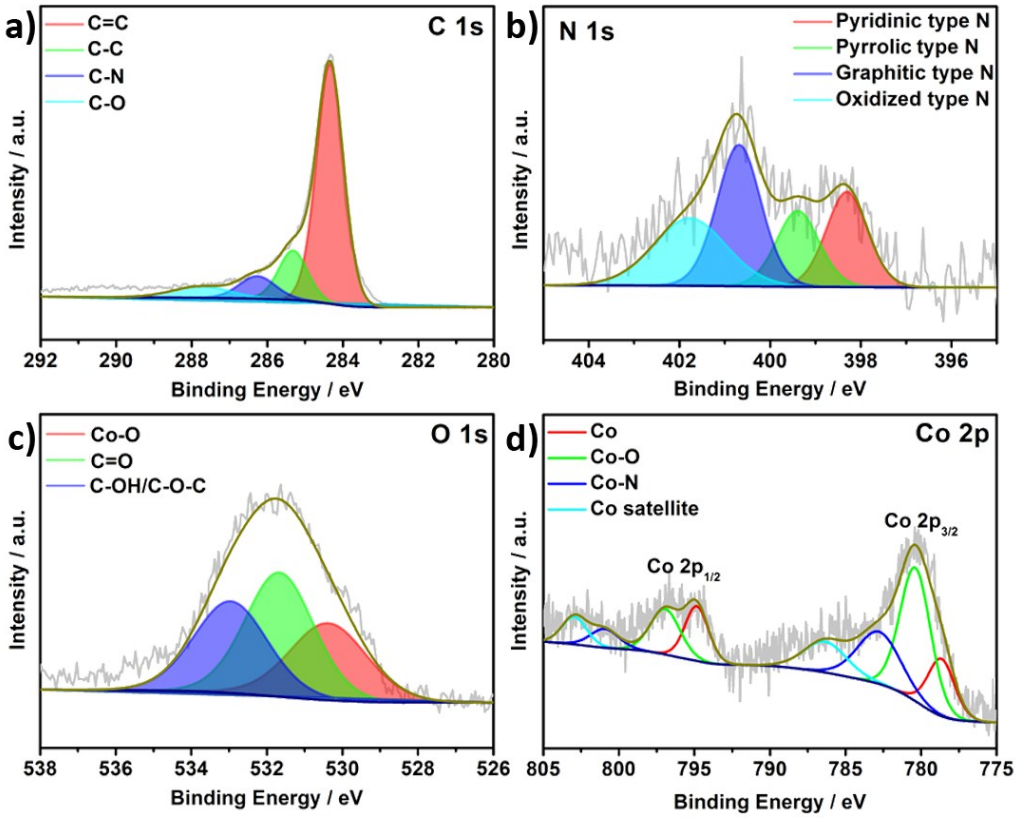

Figure S8. The high-resolution XPS C 1s, N 1s, O 1s, and Co 2p spectra of **Co-ZIF/CS-1000**.

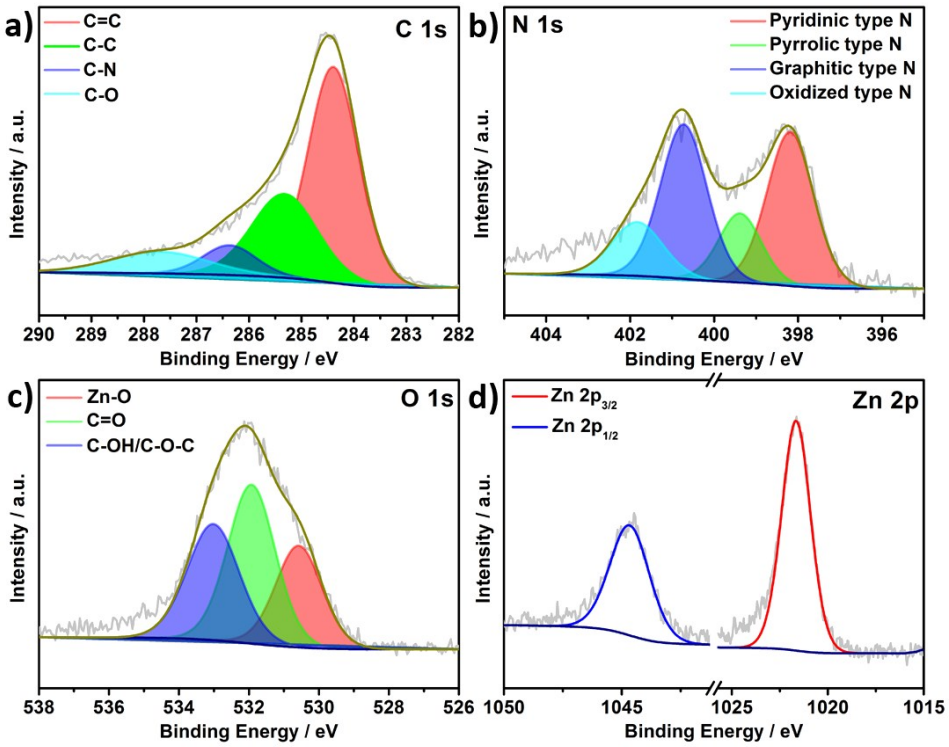

Figure S9. The high-resolution XPS C 1s, N 1s, O 1s, and Zn 2p spectra of **Zn-ZIF/CS-1000**.

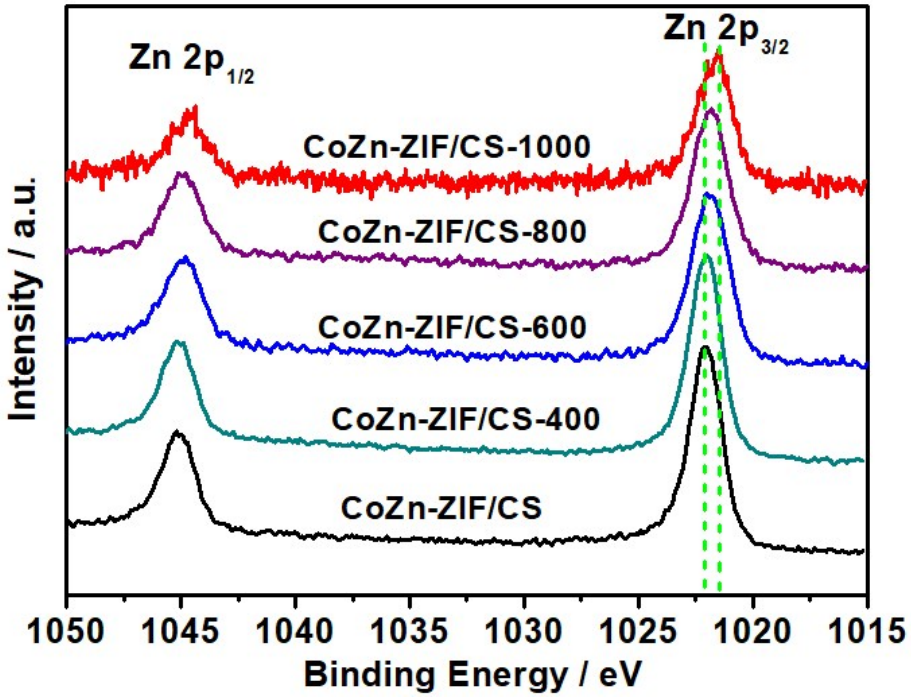

Figure S10. Deconvoluted Zn 2p XPS spectra for CoZn-ZIF/CS series at different temperatures.

The Zn $2p_{3/2}$ peak at a binding energy of 1022.1 eV in CoZn-ZIF/CS remains unchanged, which is in good agreement with the Zn cation with a valence of +2. At high temperatures, the complete decomposition (400 ^{o}C) to carbonization (1000 ^{o}C) shows a gradual shift in the Zn 2p peak position from 1022.0 eV to 1021.6 eV in **Figure S10**, which indicates the transformation of Zn(II) to metal Zn(0).

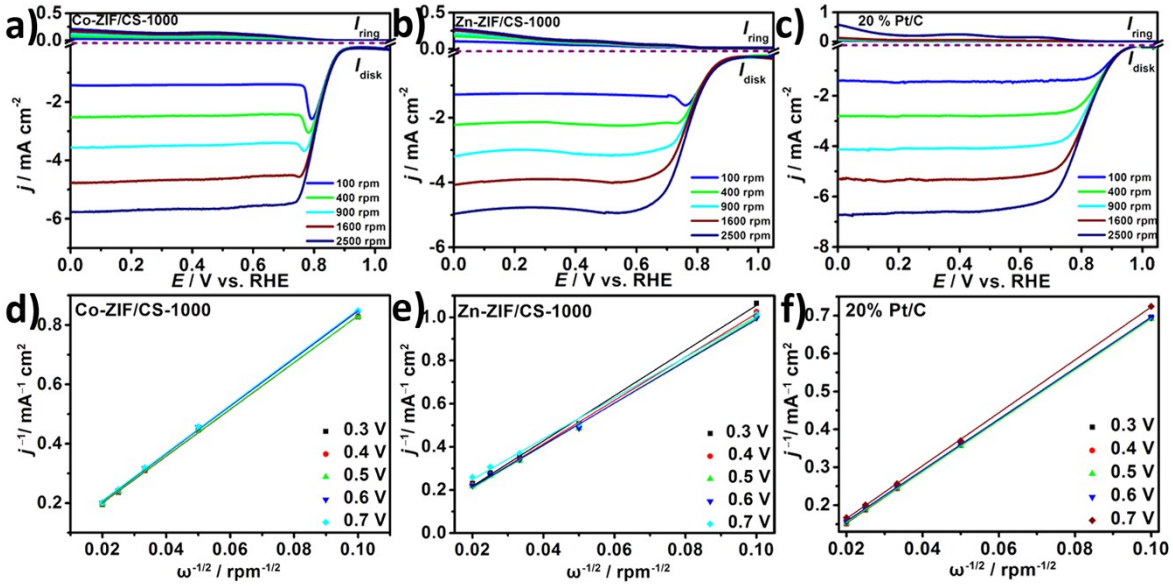

Figure S11. RRDE plots with various rotation speeds at a scan rate of 5 mV s^{-1} and Koutecky-Levich (K-L) plots at various voltages at 1600 rpm in O_2-saturated 0.1 M KOH solution of (a, d) **Co-ZIF/CS-1000**, (b, e) **Zn-ZIF/CS-1000**, and (c, f) **Pt/C**.

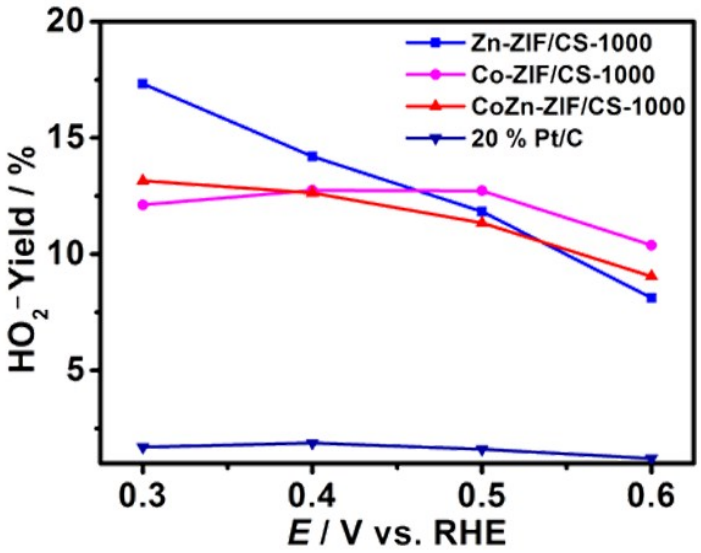

Figure S12. Hydrogen peroxide yields of the CoZn-ZIF/CS-1000, Co-ZIF/CS-1000, Zn-ZIF/CS-1000, and Pt/C in O_2-saturated 0.1 M KOH electrolyte at 1600 rpm.

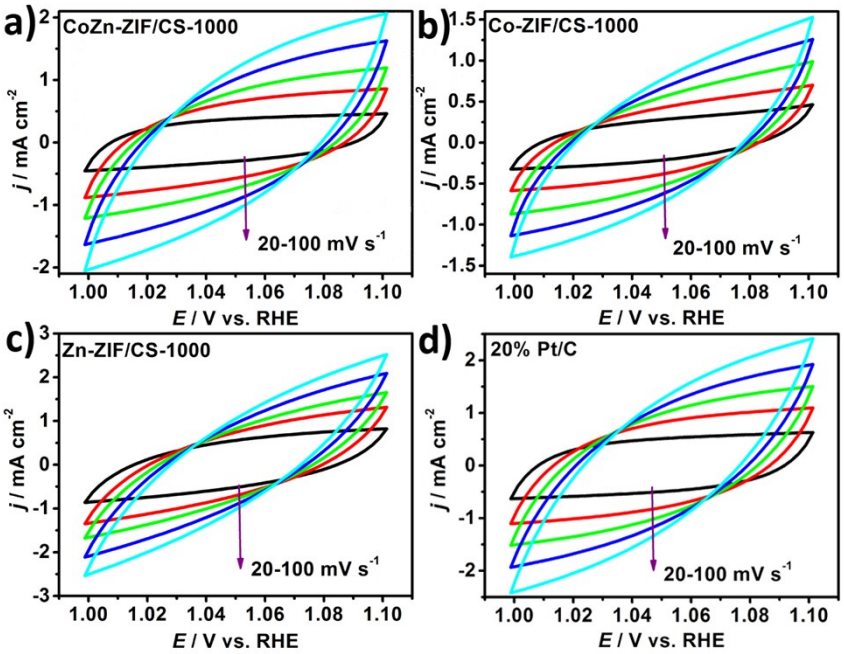

Figure S13. CV plots of the (a) **CoZn-ZIF/CS-1000**, (b) **Co-ZIF/CS-1000**, (c) **Zn-ZIF/CS-1000**, (d) **Pt/C** in 0.1 M KOH solution in the region of 1.00-1.10 V vs. RHE for ORR.

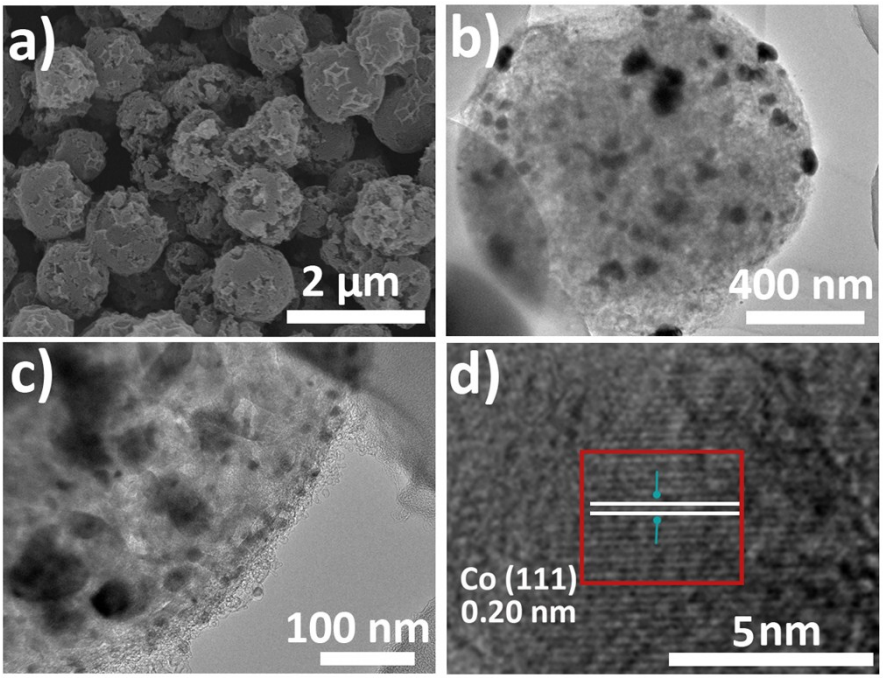

Figure S14. (a) SEM, (b) TEM, and (c, d) HR-TEM images of CoZn-ZIF/CS-1000 after ORR stability test for 10 h.

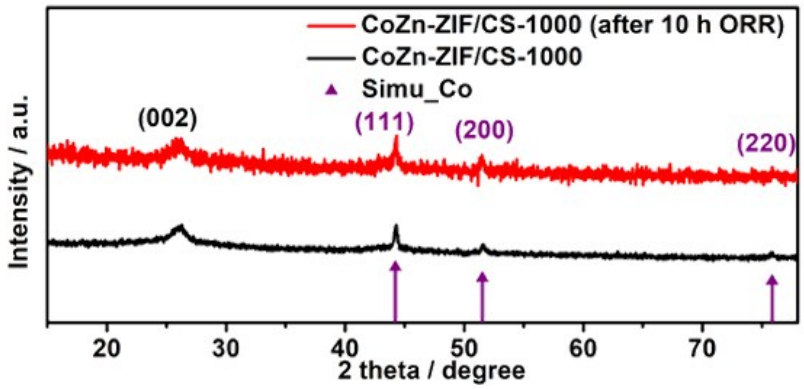

Figure S15. PXRD patterns of CoZn-ZIF/CS-1000 before (Black) and after (Red) ORR stability test for 10 h.

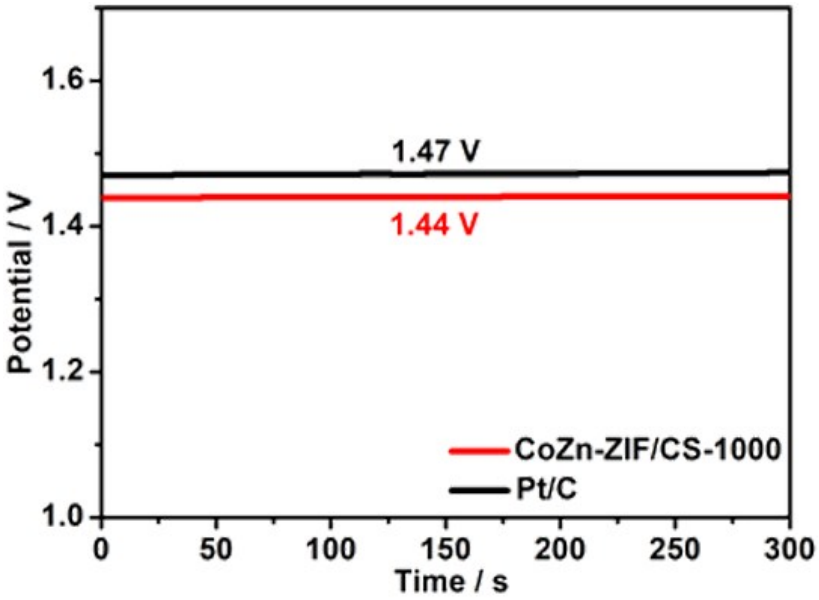

Figure S16. Open circuit voltage curves of Zn-air batteries with different **CoZn-ZIF/CS-1000** material and Pt/C.

Tables S1. Pore characteristics of all samples mentioned in the main article.

Sample	Surface area/m^2g^{-1}		Total pore volume[a]/cm^3g^{-1}	Micropore volume[b]/cm^3g^{-1}	$V_{meso+macro}/V_{micro}$
	BET method	Langmuir method			
CS	1336	1748	0.67	0.53	0.26
PDA/CS	159	128	0.09	0.06	0.56
Co-ZIF/CS	311	355	0.15	0.12	0.25
Zn-ZIF/CS	638	713	0.26	0.25	0.03
CoZn-ZIF/CS	500	558	0.21	0.19	0.06
Co-ZIF/CS-1000	354	386	0.36	0.05	6.08
Zn-ZIF/CS-1000	1015	1303	0.57	0.24	1.34
CoZn-ZIF/CS-1000	586	625	0.39	0.11	2.44

Table S2. C, N contents and N dopant proportions of **CoZn-ZIF/CS-1000**, **Zn-ZIF/CS-1000**, and **Co-ZIF/CS-1000** catalysts measured from fitting of the N 1s XPS.

Sample	C 1s /wt%	N 1s /wt%	Relative content of differernt N species /%				$N_{effective}$ /N_{total} /%
			pyridinic-N	pyrrolic-N	graphitic-N	oxidized-N	
CoZn-ZIF/CS-1000	85.82	3.44	30.07	19.64	28.33	21.96	58.4
Co-ZIF/CS-1000	89.46	2.94	22.43	17.69	34.01	25.87	56.44
Zn-ZIF/CS-1000	90.74	2.80	29.71	20.64	29.71	19.93	59.42

Tip: $N_{effective}=N_{pyridinic\text{-}N}+N_{graphitic\text{-}N}$

Table S3. Comparison of ORR performance for **CoZn-ZIF/CS-1000** with reported carbon-based electrocatalysts.

Catalyst	E_{onset} (V vs RHE)	$E_{1/2}$ (V vs RHE)	n^e	$\|J_L\|$ (mA cm-2)	Reference
C-CZ-4-1000	1.03	0.89	3.99	5.9	[S1]
VNHSs	0.83	-	3.9	5.5	[S2]
Co-C@NWCs	0.94	0.83	3.99	4.51	[S3]
MMo_2C/NCS	0.92	0.83	3.5	4.48	[S4]
meso/micro-FeCo-N_x-CN-30	-	0.89	-	6.3	[S5]
CoHNCS-0.2	0.94	0.82	3.84	5.8	[S6]
Fe-N-RFC_C240	0.998	0.91	3.99	5.48	[S7]
A-NHCN-800	0.9	0.81	3.9	3.63	[S8]
Fe-N-C HNSs	1.046	0.84	3.98	5.8	[S9]
FeNC-950	0.94	0.84	3.95	5.85	[S10]
CoZn-ZIF/CS-1000	0.93	0.82	3.82	5.11	**This work**

References

[S1] L. Ge, Y. Yang, L. Wang, W. Zhou, R. D. Marco, Z. G. Chen, J. Zou, Z. H. Zhu, High activity electrocatalysts from metal-organic framework-carbon nanotube templates for the oxygen reduction reaction, Carbon 2015, 82, 417-424.

[S2] D. Zhao, Z. T. Cui, S. G. Wang, J. W. Qin, M. H. Cao, VN hollow spheres assembled from porous nanosheets for high-performance lithium storage and the oxygen reduction reaction, J. Mater. Chem. A 2016, 4, 7914-7923.

[S3] Y. Y. Li, F. Y. Cheng, J. N. Zhang, Z. M. Chen, Q. Xu, S. J. Guo, Cobalt-Carbon Core-Shell Nanoparticles Aligned on Wrinkle of N-Doped Carbon Nanosheets with Pt-Like Activity for Oxygen Reduction, small 2016, 12, 2839-2845.

[S4] Y. N. Guo, J. Tang, J. Henzie, B. Jiang, H. Y. Qian, Z. L. Wang, H. B. Tan, Y. Bando, Y. Yamauchi, Assembly of hollow mesoporous nanoarchitectures composed of ultrafine Mo_2C nanoparticles on N-doped carbon nanosheets for efficient electrocatalytic reduction of oxygen, Mater. Horiz. 2017, 4, 1171-1177.

[S5] S. Li, C. Cheng, X. J. Zhao, J. Schmidt, A. Thomas, Active Salt/Silica-Templated 2D Mesoporous FeCo-Nx-Carbon as Bifunctional Oxygen Electrodes for Zinc-Air Batteries, Angew. Chem. Int. Ed. 2018, 57, 1856-1862.

[S6] X. D. Chen, K. Shen, J. Y. Chen, B. B. Huang, D. N. Ding, L. Zhang, Y. W. Li, Rational design of hollow N/Co-doped carbon spheres from bimetal-ZIFs for high-efficiency electrocatalysis, Chemical Engineering Journal 2017, 330, 736-745.

[S7] M. Kim, H. S. Kim, S. J. Yoo, W. C. Yoo, Y.-E. Sung, The role of pre-defined microporosity in catalytic site formation for the oxygen reduction reaction in iron- and nitrogen-doped carbon materials, J. Mater. Chem. A 2017, 5, 4199-4206.

[S8] B. He, F. J. Liu, Y. Liu, S. Yan, Development of g-C_3N_4 activated hollow carbon spheres with good performance for oxygen reduction and selective capture of acid gases, Electrochimica Acta 2019, 324, 134869.

[S9] Y. F. Chen, Z. J. Li, Y. B. Zhu, D. M. Sun, X. E. Liu, L. Xu, Y. W. Tang, Atomic Fe Dispersed on N-Doped Carbon Hollow Nanospheres for High-Efficiency Electrocatalytic Oxygen Reduction, Adv. Mater. 2019, 31, 1806312.

[S10] Y. M. Ma, S. S. Luo, M. H. Tian, J. E. Lu, Y. Peng, C. Desmond, Q. M. Liu, Q. X. Li, Y. L. Min, Q. J. Xu, S. W. Chen, Hollow carbon spheres codoped with nitrogen and iron as effective electrocatalysts for oxygen reduction reaction, Journal of Power Sources 2020, 450, 227659.